KONA Powder and Particle Journal

KONA Powder and Particle Journal No. 43 (2026) 310–322/https://doi.org/10.14356/kona.2026005 Original Research Paper

Effect of Design Parameters on Flow Characteristics in Powder Supply System for Micropropulsion Systems †

Masaya Murohara [1,2]*, Marius C. Banica [1], Hiroyuki Koizumi [3] and Matteo Madi [2]

[1] *Institute of Energy Systems and Fluid-Engineering, Zurich University of Applied Sciences, Switzerland*
[2] *Sirin Orbital Systems AG, Switzerland*
[3] *Department of Advanced Energy, The University of Tokyo, Japan*

Aluminum powder is an attractive fuel, especially for micropropulsion, due to its wide availability, high volumetric and gravimetric energy densities, and environmental friendliness. For safety reasons, the powder is preferably stored and supplied to a combustion chamber separately from the oxidizer. However, powder supply systems for micropropulsion applications are technologically immature. To improve this situation, a powder supply system was developed, and the impacts of important design factors on the supply characteristics were studied. This included operating modes, carrier gas pressures, gas line conductances, and powder line lengths. The results showed that, when compared to continuous operation, pulsed operation achieved 1) significantly higher powder flow rates and 2) significantly higher ratios of powder to carrier gas mass flow rates, ϕ. Furthermore, higher carrier gas pressures can increase the powder mass flow rates, but this reduces ϕ. The gas line conductance had a lesser impact on the powder flow rates than the pressure, but increasing the former also increased the powder flow rates without significant impact on ϕ. The powder line length had a negative impact on the powder flow rate, but no significant impact on ϕ. These results will help the future development of micropropulsion systems that use powder fuels.

Keywords: pneumatic transfer, pulsed supply system, poor fluidity powder, pinch-type valve, micropropulsion system

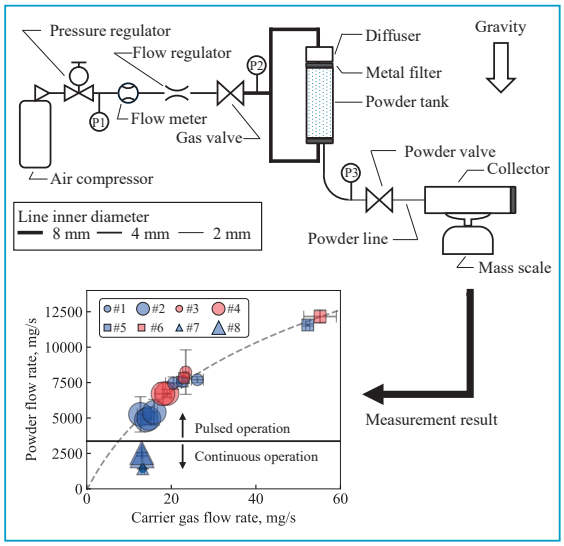

1. Introduction

Aluminum powder is an attractive fuel due to its high availability, high volumetric and gravimetric energy densities, and environmental friendliness (David and Knoll, 2017; Foote et al., 2001; Miller et al., 2002; Murohara et al., 2024; Risha et al., 2014; Wollmark and Yavor, 2019). Due to the possibility of *in situ* resource utilization (ISRU) on the moon, it is particularly interesting as a propellant for small spacecraft. For instance, Wollmark and Yavor demonstrated a solid rocket motor (SRM) that used nano-sized aluminum particles and liquid water as propellants (Wollmark and Yavor, 2019), while Risha et al. used nano-sized aluminum particles and frozen water (Risha et al., 2014). These SRMs are promising; however, Nishii and Koizumi pointed out that SRMs reduce safety, and the fuel and oxidizer ideally should be stored and supplied separately (Nishii and Koizumi, 2024). Based on this idea, Murohara et al. studied the combustion of micron-sized aluminum and water vapor (Murohara et al., 2024). In their study, the powder was inserted into the combustion chamber in advance because the employed powder supply system was technologically immature.

Powder supply from one place to another (e.g., from a storage tank to a reaction tank, from a silo to the back of a truck, etc.) is an important technology in various fields such as industry, agriculture, and medicine. However, most of the powder supply systems cannot be used in space because they use gravity (Besenhard et al., 2017; Ruiz-Carcel et al., 2018). For space applications, a commonly used method is pneumatic supply, which uses a carrier gas to fluidize and transfer the powder (Li et al., 2021; Miller and Herr, 2004; Sun et al., 2016).

Pneumatic supply systems are typically assessed by either pressure drop or the ratio of powder to gas mass flow rate, ϕ (Morikawa, 1991). Pressure drops are typically in the range of 0.1–10 kPa/m (Morikawa, 1991). The pressure drop is a critical performance parameter in industrial applications where transfer distances span several tens or hundreds of meters. In contrast, the transfer distance in

† Received 25 September 2024; Accepted 18 November 2024
J-STAGE Advance published online 25 March 2025
* Corresponding author: Masaya Murohara;
[1] Add: Technikumstrasse 9, Winterthur 8401, Switzerland
[2] Add: Genferstrasse 24, Zurich 8002, Switzerland
E-mail: masayamurohara@gmail.com
TEL: +41 (0) 58 934 41 72

micropropulsion systems is much shorter, making the pressure drop less significant. Instead, ϕ is the major performance parameter for micropropulsion. Lower values mean that larger amounts of gas must be loaded, and so maximizing ϕ is crucial to obtain adequate overall system performance.

In addition to ϕ, there are three other important factors from the viewpoint of combustion: powder mass flow rate (hereinafter called powder flow rate), powder velocity, and available particle size. The powder flow rate directly impacts combustion because it can be used to adjust the oxidizer-fuel mass ratio. For micropropulsion systems, the required powder flow rates are lower than those in industrial applications, specifically, about 1 g/s, because of the small combustion chambers used. After ignition, the powder must react as much as possible. Thus, the powder velocity should be low enough to complete the reaction within the combustion chamber. Finally, particle sizes below 100 μm are required to achieve short ignition delays (Sundaram et al., 2015) and, thereby, maximize thrust. However, micron-sized or smaller aluminum powder generally has poor fluidity. As a result, it is difficult to simultaneously meet all requirements described above.

Powder fluidity was categorized by Geldart (1973) into different groups. Aluminum powder smaller than 100 μm tends to show characteristics of Geldart group C. Because cohesive forces are dominant in this type, it is prone to form a rat hole, resulting in supply difficulties (Cocco and Chew, 2023; Qian et al., 2001). In a study of Geldart group C powder, Ogata overcame this difficulty for stable supply by injecting a carrier gas from two directions: top and bottom of the powder bed (Ogata, 2019). Also, Xu et al. pointed out that introducing a pulsed gas into a powder bed contributes to stabilizing the fluidization by breaking up agglomeration (Xu et al., 2022). These previous studies imply that supply of Geldart group C powders is feasible with minor modifications, but there is still a lack of knowledge about the effects of parameters such as carrier gas pressure and supply line lengths. These parameters are particularly important for designing a practical micropropulsion powder supply system.

The purpose of the present study was to investigate the effect of pulsed supply characteristics on the lower limits of flow rates for micron-sized aluminum powder. This constitutes a first step in the design of powder supply systems for micropropulsion applications, and the technology readiness level is low. As a result, the experiments were carried out under $1g_0$ and not under microgravity conditions. Important design parameters include carrier gas pressures, gas line conductances, and powder line lengths. We developed a system that can supply 10 μm-class aluminum powders in pulsed operation. Powder flow rates were measured, and the ratio ϕ and the powder velocity were estimated.

2. Experimental setup

2.1 Overview

A schematic representation of the experimental setup is shown in **Fig. 1**. The aluminum powder was stored in a powder tank and fluidized by the carrier gas, air, which was supplied by a compressor. The flow of the air–powder mixture was regulated by a powder valve. The discharged aluminum powder was collected in a collector tank. Its mass change was monitored by a mass scale.

The carrier gas pressure was adjusted to a target value by a pressure regulator (Model 10, Fairchild Products). System pressures were measured by three sensors (P1, P2, and P3 in **Fig. 1**; AP-43, KEYENCE) with a measurement range of 0–1,000 kPa and accuracy of ±0.33 kPa (1σ). The sensors were located downstream of the pressure regulator (P1), as well as upstream (P2) and downstream (P3) of the powder tank. The flow conductance of the carrier gas line was controlled by a flow regulator (SS-22RS6MM, WHITELY). The conductance is a coefficient that relates the pressure difference and the mass flow rate of a gas (JIS B2005-1, 2004), which is mainly determined by the smallest cross-sectional area of the flow line. By determining the conductance and the upstream and downstream pressure, the carrier gas mass flow rate can be regulated. The carrier gas mass flow rate (hereinafter called gas flow rate) was measured by a flow meter (SFAH-1U, FESTO) with a measurement range of 0–19.3 mg/s and accuracy of ±0.05 mg/s (1σ). The carrier gas supply was regulated by a gas valve (VXD230AA, SMC), which was kept open during experimental runs.

The carrier gas line had a branch upstream of the powder tank. One branch connected to the top and the other connected to the bottom. The carrier gas from both branches flowed into the powder tank through sintered metal filters with a mesh size of 20 μm (INFICON). In **Fig. 2**, the geometry around the lower carrier gas inlet is shown. The left picture illustrates the carrier gas supply path, and the path on which the carrier gas/metal powder mixture is evacuated (white arrow). The right picture shows the physical situation. Note that the inlet (the sintered metal filter) is an annular surface, and that the carrier gas was supplied to the filter through an annular channel. The carrier gas lines had

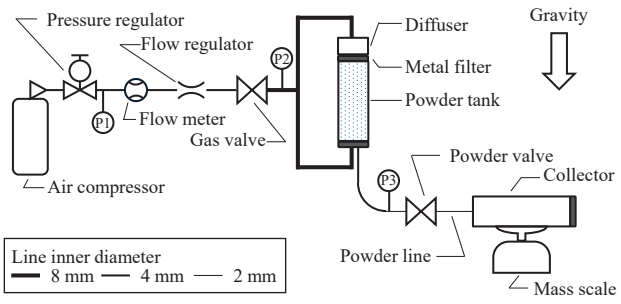

Fig. 1 Schematic of the experimental setup. The symbols P1, P2, and P3 represent the pressure sensors.

inner diameters of 8 mm, and the powder tank had an inner diameter of 23 mm and an inner height of 100 mm (cf. **Table 1**). The tank was equipped with a diffuser at the top with an inner diameter of 23 mm and a length of 40 mm. This two-way supply system was developed based on a previous study by Ogata et al. (Ogata and Ariga, 2021), who reported that such a setup can discharge Geldart group C powder stably without the formation of rat holes.

The tank outlet (marked by the center arrow in **Fig. 2(B)**) had an inner diameter of 4 mm and was connected to the powder line. The latter was made of silicon (PUTC4, MISUMI) with an inner diameter of 2 mm and a wall thickness of 1 mm. Its shore hardness and Young's modulus were 70 A and 5.2 MPa, respectively. The powder line was routed through the powder valve, which was a pinch-type design. The powder line length between the collector tank and the pinch valve was one of the parameters that were varied in this study. This length did not affect the carrier gas line conductances. The pinch valve controlled the flow (on/off) by pinching the silicone line. The details of the powder valve are described in **Section 2.2**. When the powder valve opened, the aluminum powder was shot to the collector tank that had an inner diameter of 26.2 mm and an inner length of 120 mm. It also had the same filter as the ones that powder tank was equipped with. The collector tank was open to the room through the filter. The aluminum powder was collected there, and the mass change of the collector tank was measured by a mass scale (MS 1602S, METTLER TOLEDO) that had a resolution of 10 mg and settling time of 1 s.

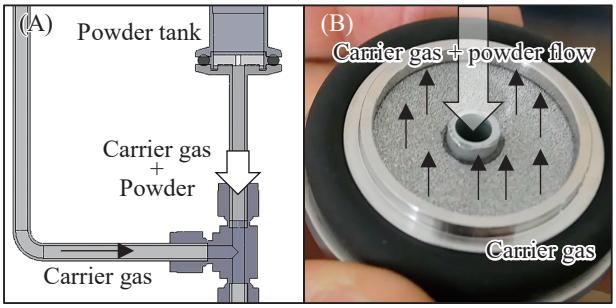

Fig. 2 **(A)** Enlarged half-sectional view of a CAD model of the lower part of the powder tank, and **(B)** the appearance of the carrier gas inlet and outlet for the carrier gas/metal powder mixture.

Table 1 Common experimental conditions.

Powder tank internal geometry	Diameter: 23 mm, Length: 100 mm
Powder line inner diameter	2 mm
Initial powder mass	29.9 ± 0.7 g
Initial powder tank voidage	0.70 ± 0.01
Carrier gas	Air
Injection frequency in pulsed operation	0.25 Hz
Total valve opening time in pulsed operation	140 ms

Special care had to be taken when evaluating the gas flow rate in pulsed operation. The gas flow rate at the gas valve was mainly determined by the conductance of the flow regulator and the pressure difference between the carrier gas and powder tank. On the other hand, the gas flow rate at the powder valve was determined by the conductance of the powder line and pressure difference between the powder tank and the collector tank. Therefore, the flow rate measured by the flow meter was equal to the gas flow rate at the powder valve only when the supply was in continuous operation. When the supply was in pulsed operation, there was a difference between the two flow rates. What we were able to determine in pulsed operation was an integrated discharged gas mass from the measured gas flow rate in one pulse.

The behavior of the powder in the powder tank was observed with a transparent tank made of PMMA. It should be noted that this transparent tank was used only for the observation test, and the main experimental runs were carried out with the metal powder tank because we wanted to eliminate the effects of static electricity on the experimental results. Sequential pictures for powder supply in pulsed operation are shown in **Fig. 3**. The time interval between each picture is 10 s. The powder bed was settled at the bottom of the powder tank and the powder was not stirred up significantly by the gas flow. The powder bed surface was lowered by the supply of carrier gas and powder to the collector tank. The pictures indicate that the experimental setup worked as expected. Rat holes were not observed in any test.

2.2 Powder valve

The powder valve had a pinch-type design to maximize the powder valve conductance and avoid potential issues with powder clogging around sealings (Oh et al., 2005). A CAD-based representation of the valve is shown in **Fig. 4**. It consisted of a housing, a solenoid magnetic actuator with a pinch plunger (M590C-22P, SHINDENGEN), a plunger cover, and four springs (WL-14-40, MISUMI). The housing and plunger cover were made of 3D printed ABS. The powder valve closed the powder line by pinching it with the

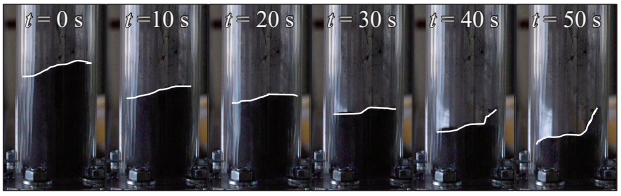

Fig. 3 Sequential pictures during the powder supply in pulsed operation. The powder tank was made of PMMA specified for this observation. The white lines indicate the surface of the powder bed.

plunger.

The pinch valve was normally open, and the valve closed when an electrical current was applied. The closing force, F, of the valve can be estimated from a force vs. ampere-turn map provided by the supplier of the actuator. The ampere-turn is calculated by IN, where I is the electric current and N is number of turns of the coil. In our experiments, $I \approx 3$ A, $N = 336$, and so $F \approx 100$ N with a stroke of 3 mm. When the power supply was turned off, the springs pushed up the plunger, and the powder valve opened. Their spring constant was 1 mm/N, and natural length was 40 mm. The powder valve was operated by a signal from a function generator (AFG2021, Tektronix). The power consumption of the valve was not optimized in this valve. It depended on the operation frequency and the valve closing time. The power consumption can be significantly reduced by operating the valve in reverse mode, i.e., using an electric current to open a normally closed valve.

The response time of the powder valve was evaluated by measuring the gas flow rate immediately downstream of the pinch valve. For this measurement, the branched powder line, diffuser, powder tank, and collector tank were removed from the experimental setup shown in Fig. 1. The gas valve was directly connected to the pinch valve, and the flow sensor was moved to immediately downstream of the pinch valve. The time lag between the commencement of the valve signal and the peak in gas flow rate was 20 ms. The time lag between the start of valve signal cessation and the reduction of the gas flow rate to zero was 40 ms. The opening and closing response times were hence 20 ms and 40 ms, respectively. The total time of valve opening, τ_{open}, can hence be calculated from the sum of the valve opening time, the valve closing time, and the time during which the valve remained in the fully open position.

The time during which the valve remained in the fully open position should be longer than the opening and closing time, or the powder flow cannot reach a stable state. On the other hand, the powder supply time should be short compared to the combustion time of the aluminum powder in the combustion chamber. Murohara et al. reported that the reaction time of aluminum and water vapor combustion took several hundred milliseconds (Murohara et al., 2024). Given this, we chose 140 ms as the powder valve opening time, out of which 20 ms was for valve opening, 80 ms for the valve in the fully open position, and 40 ms for valve closing.

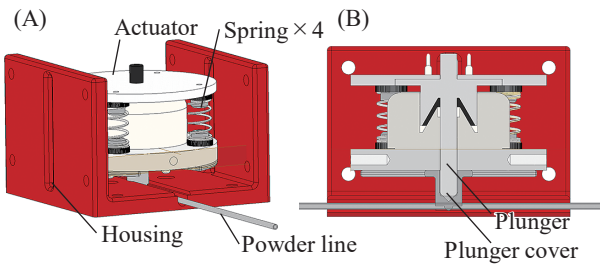

Fig. 4 CAD-based drawing of the powder valve. **(A)** Isometric view and **(B)** Cross-sectional view.

2.3 Aluminum powder

Fig. 5 shows a scanning electron microscope (SEM) image of the aluminum powder used (Pyro 5413H Super, Laborladen). Clearly, the powder was non-spherical. Its particle size distribution (PSD) was measured by dynamic image analysis (CAMSIZER X2, MicrotracBEL Corp.), and the results are shown in Fig. 6. In the figure, d_x represents the diameter of the x^{th} percentile in the PSD. The size polydispersity σ_d was 2.27, and was determined from

$$\sigma_d = (d_{90} - d_{10}) / d_{50} \tag{1}$$

Since $d_{50} = 13.74$ μm, the powder was in Geldart group C, i.e., had high cohesiveness and poor fluidity. The solid line in Fig. 6 represents the cumulative PSD.

2.4 Experimental procedure and conditions

The initial aluminum powder mass in the powder tank was $m_{Al,ini} = 29.9$ g with voidage $\varepsilon_t = 0.70$. The latter was calculated from

$$\varepsilon_t = 1 - \frac{4m_{Al,ini}}{\pi d_t^2 h \rho} \tag{2}$$

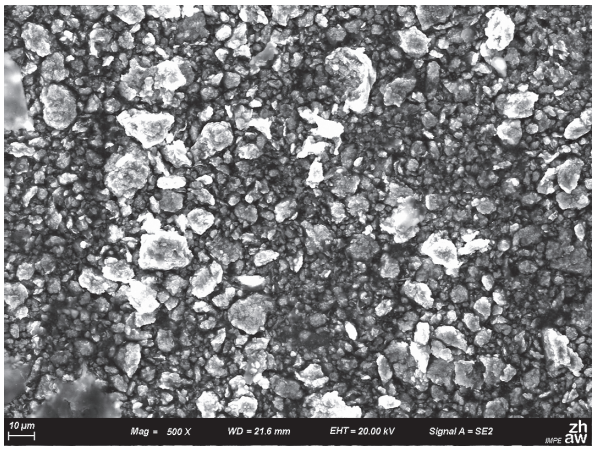

Fig. 5 SEM images of the aluminum powder.

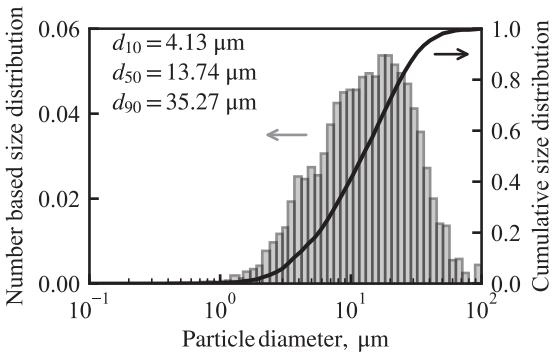

Fig. 6 Particle size distribution.

Table 2 Variable experimental conditions.

No.	Gas pressure [kPa]	Gas line conductance [kg/ (Pa s)]	Powder line length [mm]	Operation
1	190	1.47×10^{-11}	284	Pulsed
2	190	1.47×10^{-11}	331	Pulsed
3	190	2.94×10^{-11}	284	Pulsed
4	190	2.94×10^{-11}	331	Pulsed
5	280	1.47×10^{-11}	284	Pulsed
6	280	2.94×10^{-11}	284	Pulsed
7	190	1.47×10^{-11}	284	Continuous
8	190	1.47×10^{-11}	331	Continuous

where $d_t = 23$ mm is the inner diameter of the powder tank, h is the height of the powder bed, and $\rho = 2{,}710$ kg/m^3 is the mass density of aluminum.

In the experiments, powder was supplied in both continuous and pulsed modes. The powder valve remained open during continuous operation, whereas it repeatedly opened and closed in pulsed mode.

For the pulsed mode, five powder valve open–close cycles were completed before starting the carrier gas supply. This step was required to reduce an inaccuracy in the mass measurement that was due to shocks generated by the valve closing. The mass reading of the scale changed in reaction to these shocks, but the changes became reproducible after five open–close cycles. This settling-in period was probably caused by the change of tension of the powder line, which was minimized after five cycles. Upon completion of these five cycles, the carrier gas valve was opened. The supplied carrier gas then fluidized the aluminum powder in the tank and transferred it downstream, thereby effectively filling the powder line with a carrier gas/powder mixture. The powder valve was then opened, upon which aluminum powder was injected into the collector tank. The powder valve continued to operate until the value on the mass scale stopped changing regardless of the operation modes.

Eight experimental runs were conducted in total. **Table 1** contains the experimental parameters that were common to all runs, while **Table 2** contains the parameters that were varied between the runs.

2.5 Definition of the mass ratio ϕ

We used the ratio of injected powder mass to carrier gas mass, ϕ, to compare the two operation modes. In continuous operation, the collector tank mass time history was, in good approximation, linear (cf. **Fig. 7** and description in **Section 3.1**). Using the slope, the average powder flow rate, $\dot{m}_{\mathrm{cont,p}}$, can be calculated from

$$\overline{\dot{m}}_{\mathrm{cont,p}} = \frac{m_{\mathrm{c}}(t_{\mathrm{e}}) - m_{\mathrm{c}}(t_{\mathrm{s}})}{t_{\mathrm{e}} - t_{\mathrm{s}}} \tag{3}$$

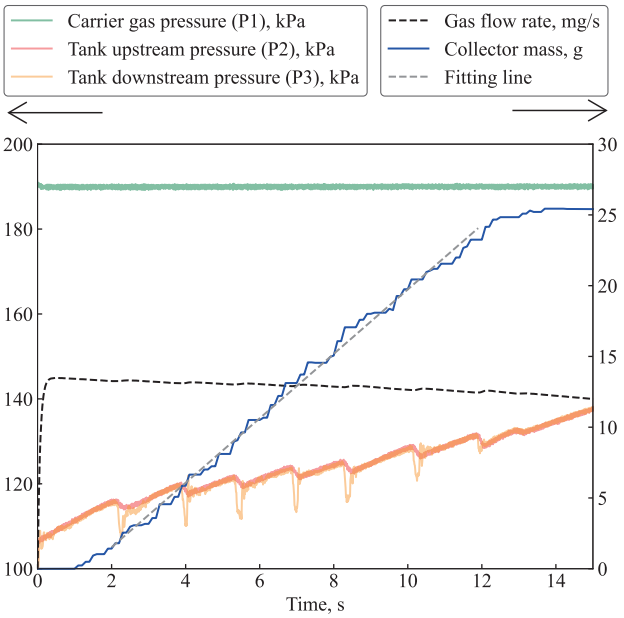

Fig. 7 Time histories of various parameters in experiment #8 (continuous operation). See **Fig. 1** for location of pressure sensors P1, P2, and P3.

where t_{s} and t_{e} are the times when the continuous powder injection started and ended, respectively. The time-dependent carrier gas flow rate in continuous operation, $\dot{m}_{\mathrm{cont,g}}$, was obtained from the flow meter readings, $\dot{m}_{\mathrm{g}}$, and so

$$\dot{m}_{\mathrm{cont,g}} = \dot{m}_{\mathrm{g}} \tag{4}$$

The averaged carrier gas flow rate, $\overline{\dot{m}}_{\mathrm{cont,g}}$, in continuous operation is

$$\overline{\dot{m}}_{\mathrm{cont,g}} = \int_{t_{\mathrm{s}}}^{t_{\mathrm{e}}} \dot{m}_{\mathrm{g}} \mathrm{d}t \,/\, (t_{\mathrm{e}} - t_{\mathrm{s}}) \tag{5}$$

The time-averaged ratio of injected powder mass to carrier gas mass in continuous operation, $\overline{\phi}_{\mathrm{cont}}$, can then be defined as

$$\overline{\phi}_{\mathrm{cont}} \equiv \overline{\dot{m}}_{\mathrm{cont,p}} \,/\, \overline{\dot{m}}_{\mathrm{cont,g}} \tag{6}$$

In pulsed operation, the injected powder mass in the i^{th} pulse, $m_{\mathrm{pulse,p},i}$, is calculated from

$$m_{\mathrm{pulse,p},i} = m_{\mathrm{c},i+1} - m_{\mathrm{c},i} \tag{7}$$

where $m_{\mathrm{c},i}$ and $m_{\mathrm{c},i+1}$ are the collector tank masses averaged over the 1 s interval preceding the i^{th} and the $(i+1)^{\mathrm{th}}$ powder valve opening, respectively. Assuming that the powder flow rate through the powder valve was constant during one shot gives

$$\dot{m}_{\mathrm{pulse,p},i} = m_{\mathrm{pulse,p},i} \,/\, \tau_{\mathrm{open}} \tag{8}$$

Multiple shots were performed in each experimental run, from which we calculated the average injected powder mass per pulse, $\overline{m}_{\mathrm{pulse,p}}$. However, we observed transitory

behavior over the first few shots, after which a steady state was reached, where the injected powder mass in each shot scattered around a mean. This observation is discussed in detail in Section 3.2 below. As a result of the transitory behavior, we removed the first several shots from the calculation of $\bar{m}_{\mathrm{pulse,p}}$. Using steady-state data only, the final value was obtained from

$$\bar{m}_{\mathrm{pulse,p}} = \Sigma_{i=n_\mathrm{m}}^{n_\mathrm{n}} m_{\mathrm{pulse,p},i} / (n_\mathrm{n} - n_\mathrm{m}) \tag{9}$$

where n_m and n_n are the first and last pulse numbers of the steady state, respectively.

The steady state was judged by the injected carrier gas mass, which for the i^{th} pulse was calculated from

$$m_{\mathrm{pulse,g},i} = \int_{t_i}^{t_i+\tau_\mathrm{open}} \dot{m}_\mathrm{g} \mathrm{d}t \tag{10}$$

where t_i is the time instant of the i^{th} powder valve opening, and $\dot{m}_\mathrm{g}$ is the gas flow rate measured by the flow meter. As described in Section 2.1, there was a difference between the gas flow rates at the flow meter and the powder valve. Therefore, the gas flow rate at the powder valve $\dot{m}_{\mathrm{pulse,g},i}$ was estimated as

$$\dot{m}_{\mathrm{pulse,g},i} = m_{\mathrm{pulse,g},i} / \tau_\mathrm{open} \tag{11}$$

Following Eqn. (9), the average injected carrier gas mass per pulse, $\bar{m}_{\mathrm{pulse,g}}$, was calculated from

$$\bar{m}_{\mathrm{pulse,g}} = \Sigma_{i=n_\mathrm{m}}^{n_\mathrm{n}} m_{\mathrm{pulse,g},i} / (n_\mathrm{n} - n_\mathrm{m}) \tag{12}$$

The powder and carrier gas flow rates defined by Eqns. (8) and (11) gave a mass ratio. The mass ratio in pulsed operation would appropriately be defined as the ratio of injected powder mass to gas mass in one pulse. However, in this paper, it was defined as the ratio of their flow rates in one pulse to compare the two operation modes. Thus, the ratio for the pulsed operation $\phi_{\mathrm{pulse},i}$ is

$$\phi_{\mathrm{pulse},i} \equiv \frac{\dot{m}_{\mathrm{pulse,p},i}}{\dot{m}_{\mathrm{pulse,g},i}} = \frac{m_{\mathrm{pulse,p},i}}{m_{\mathrm{pulse,g},i}} \tag{13}$$

and the average ratio is

$$\bar{\phi}_\mathrm{pulse} \equiv \left(\Sigma_{i=n_\mathrm{m}}^{n_\mathrm{n}} \bar{m}_{\mathrm{pulse,p},i} / \bar{m}_{\mathrm{pulse,g},i}\right) / (n_\mathrm{n} - n_\mathrm{m}) \tag{14}$$

Eqns. (6) and (14) were used to compare the two operation modes.

3. Results

Sections 3.1 and 3.2 show representative results for continuous and pulsed operation, experiments #8 and #1, respectively, to illustrate the procedure used for the evaluation of the experiments listed in Table 2, and to elucidate typical system behavior. Section 3.3 then presents the main results for all experiments.

3.1 Continuous operation

In Fig. 7, the time histories of several variables for experiment #8 are shown. The situation is also representative of experiment #7. The gas valve opened at time $t = 0$, and the powder valve remained open during the entire operation. The carrier gas pressure was stable at approximately 190 kPa, while the pressures upstream and downstream of the tank gradually increased. As the pressures increased, the carrier gas flow rate gradually decreased.

The collector tank mass began increasing approximately 1 s after the gas valve opening. This delay was mainly due to the delay time of the mass scale. The mass increased by approximately 25 g over a 12 s period. At $t \approx 12$ s, the collector tank mass stabilized, showing that most of the powder was discharged from the powder tank. The total powder mass discharged into the collector tank was approximately 84% of initial powder mass, $m_{\mathrm{Al,ini}}$. Linear fitting by the least squares method was done to estimate the slope of the collector tank mass-time history for the interval $2\ \mathrm{s} < t < 12$ s. From this, and Eqn. (3), we obtained $\dot{m}_{\mathrm{cont,p}} = 2.33 \pm 0.02$ g/s. The time history of $\dot{m}_\mathrm{g}$, shown graphically in Fig. 7, was used to numerically integrate the right-hand side of Eqn. (5), which yielded $\dot{m}_{\mathrm{cont,g}} = (13.1 \pm 0.2) \times 10^{-3}$ g/s. The uncertainty of $\dot{m}_{\mathrm{cont,p}}$ was derived from the measurement data, and the uncertainty of $\dot{m}_{\mathrm{cont,g}}$ was derived from the flow meter's uncertainty. Plugging both results into Eqn. (6) then resulted in $\phi_\mathrm{cont} = 177.9 \pm 2.9$.

The pressures upstream and downstream of the powder tank, P2 and P3, respectively, show discontinuous change with a period of approximately 1.8 s. The magnitude of the pressure change is larger in the downstream location, and the change stops after $t \approx 12$ s when the collector mass stabilizes. These observations suggest that voidage in the powder line decreased and the pressures increased following it. When the pressure reached a certain value, the high-density powder was pushed downstream, resulting in a temporary pressure decrease. This might imply that the flow was a plug flow, although we could not observe the powder flow itself because adhesion of the powder to the powder line walls resulted in the loss of wall transparency.

3.2 Pulsed operation

In Fig. 8, the time histories of several variables for experiment #1 are shown. Qualitatively, the situation is also representative for experiments #2–#6, which used pulsed operation as well. As described in Section 2.2, a current had to be applied to maintain the valve in the closed position. For $t < 100$ s, the pressure downstream of the powder tank shows periodic steep decreases and subsequent increases. This is apparent in the enlarged view at the top left of the figure. The timings of the pressure drops coincide with the powder valve opening signals, while the timings of the pressure rises coincide with the powder valve closing signals. The pressure decrease was probably caused by the start of the mixture flow. The increase was probably generated when the carrier gas/metal powder flow was suddenly brought to a halt by the closing of the powder valve. This is

expected to create a pressure pulse akin to the water hammer phenomenon observed in conventional hydraulic networks. Pressure peaks in P2 are much lower than those in P3, presumably because the pressure pulse was damped out by the powder in the tank while traveling upstream. This interpretation is supported by the fact that the pressure increases are smooth, rather than abrupt, after the powder injection ends, that is, for $t > 100$ s. This would be consistent with minimal to no powder transport, and hence the absence of a pressure pulse. Rather, the lines would be filled with carrier gas after the closing of the powder valve, and this results in the smooth pressure increase observed. A key observation in the figure is that the collector tank mass increased in discrete steps, which indicates successful pulsed powder supply.

Until $t \approx 39$ s, the carrier gas flow rate decreased while the pressures upstream and downstream of the tank (P2 and P3, respectively) increased. This is because the carrier gas was supplied in blow-down mode. Since the gas valve remained open throughout the experimental run, the pressures in all components located in the flow path between the gas valve and the powder valve steadily increased when the powder valve was closed. During the interval when the powder valve was open, $\tau_{open} = 0.14$ s, the carrier gas in the powder line was discharged, and the pressures dropped. Due to the flow resistance imposed by the tank, this drop was more pronounced in P3 than in P2. During the next phase, when the powder valve was in closed position, the pressure increased again. This periodic behavior was repeated until $t \approx 39$ s, when a steady state was achieved. In the steady state, the carrier gas that was supplied from the compressor to the powder line replaced the carrier gas that was discharged during powder valve opening. Therefore, there is a carrier gas flow even when the powder valve is closed. The steady state lasts until $t \approx 100$ s. From $t \approx 100$ s onwards, the carrier gas flow rate starts to increase, while the increment of the collector mass per shot is reduced. At the same time, the average pressures in P2 and P3 drop, the curve shapes align, and the oscillations are qualitatively different from those in the steady state. During the time $100 \text{ s} < t < 155$ s, the magnitude of the decrease of the flow rate varies, and signal reproducibility is difficult. Reproducibility is reestablished after $t \approx 155$ s. In summary, until $t \approx 39$ s, the supply system is in a transition state. It is in steady state during $39 \text{ s} < t < 100$ s, and then again in transition state during $100 \text{ s} < t < 155$ s. After $t \approx 155$ s, the powder tank was probably mostly empty, and the flow was a single-phase carrier gas flow.

In **Fig. 9**, as an example, the injected powder and carrier gas mass are shown for each shot for experiment #1. The error bars show the uncertainty of the mass scale and the flow meter. The inaccuracies of the mass scale were larger than the catalog specification due to the shocks associated with the closing of the powder valve (cf. **Section 2.4**). The injected carrier gas mass in **Fig. 9** was calculated by **Eqn. (10)**. This equation holds only when the supply is in the steady state. For experiment #1, **Fig. 9** shows that steady state lasted from the 10th ($t \approx 39$ s) to the 24th ($t \approx 95$ s) shot. It should be noted that each experimental run had specific shot numbers for the reaching and ending of the steady state. The 25th ($t \approx 99$ s) shot shows almost the same injected carrier gas mass as the 24th shot, but the injected powder mass decreases drastically. This implies that most of the powder was injected by the 24th shot. Focusing only on the shots in the steady state, we obtained $\bar{m}_{pulse,p} = 1044.4 \pm 61.4$ mg and $\bar{m}_{pulse,g} = 2.87 \pm 0.26$ mg.

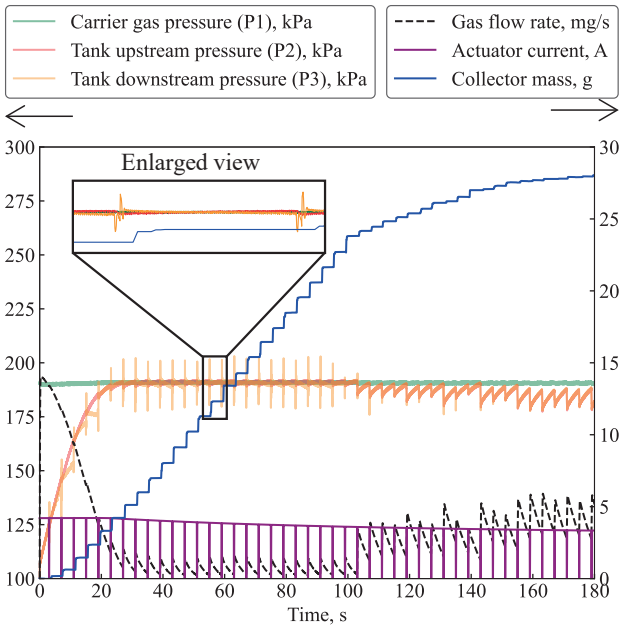

Fig. 8 Time histories of various parameters in experiment #1 (pulsed operation). See **Fig. 1** for location of pressure sensors P1, P2, and P3.

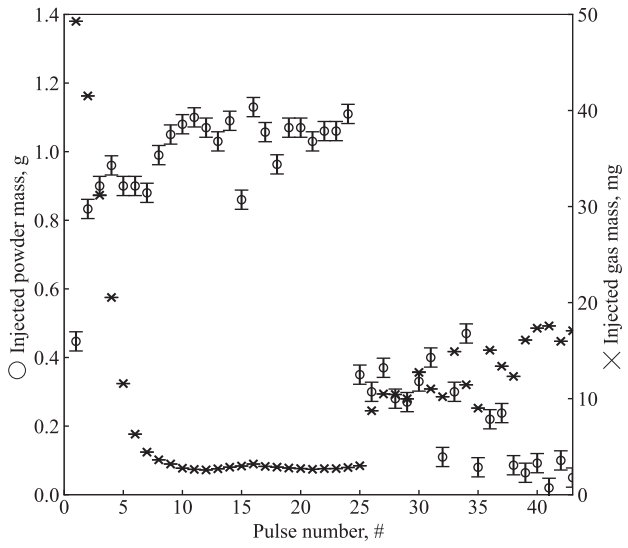

Fig. 9 Injected powder mass and carrier gas mass in each shot in experiment #1.

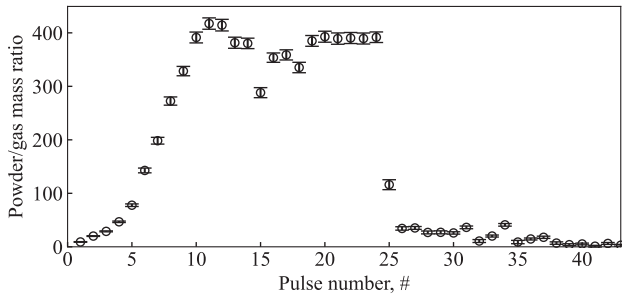

Fig. 10 Discharged powder/gas mass ratio for each shot in experiment #1.

The mass ratio for each shot in experiment #1 is shown in **Fig. 10**. During the steady state, we obtained $\phi_{\text{pulse}} = 366.8 \pm 40.4$. The uncertainties took into account the error propagation of the measurement systems and the measured values. This indicates that the gas mass constituted a mere 0.27% of the powder mass. Given that the stoichiometric mass ratio of water vapor to aluminum is unity, the injected gas mass in the propulsion system will be 0.14%, which is negligible in comparison to the water vapor and powder mass.

3.3 Flow rate and mass ratio

The relation between the powder and gas flow rates is shown graphically in **Fig. 11**. It contains the data for each experiment listed in **Table 2**, specifically, data for both pulsed and continuous operations are shown. The centers of the symbols mark the averages of the measured values. The horizontal and vertical error bars represent 1σ, where σ is the standard deviation for the experimental run. The color indicates variations in the conductance, and the symbol size indicates variations in the powder line length. The circle and square symbols indicate pulsed operation with carrier gas pressures of 190 kPa and 280 kPa, respectively. Finally, the triangles represent continuous operation. Each symbol represents the result of a single experimental run. Since some of the experiments were repeated, certain symbols appear multiple times. For pulsed operation, only data gathered during steady-state operation (cf. **Section 3.2**) were used to calculate averages and standard deviations. The average injected powder mass per pulse can be obtained from multiplying the data in **Fig. 10** by $\tau_{\text{open}} = 0.14$ s.

The dashed line in the figure shows a curve fitting for the powder flow rate in pulsed operation. The fit was obtained by constraining the curve to pass through the origin. It can be expressed as

$$\overline{\dot{m}}_{\text{pulse,p}} = \alpha_1 + \alpha_2 \log\left(\overline{\dot{m}}_{\text{pulse,g}} + \alpha_3\right), \quad (15)$$

α_1=−17778.1,
α_2=7109.3,
α_3=12.0

where α_1, α_2, and α_3 are constants obtained from the fitting. The function shows good fitting and yields a coefficient of determination of 0.98.

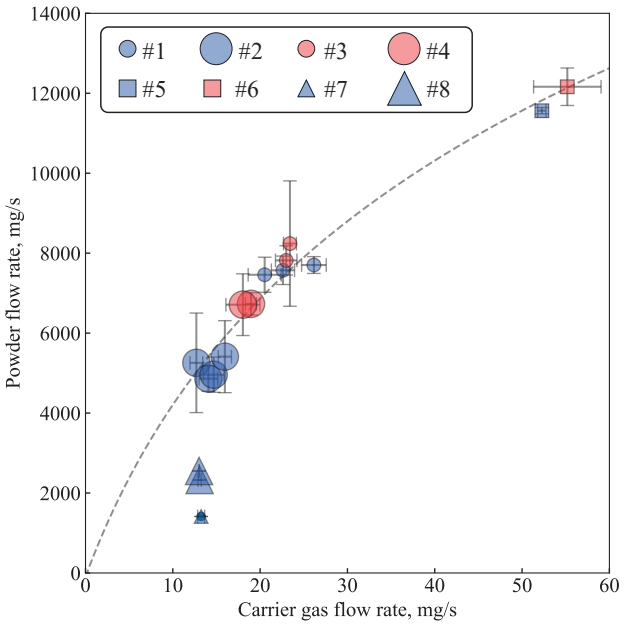

Fig. 11 Powder flow rate versus gas flow rate.

The results indicate a strong correlation between the two flow rates. Comparing experiments #1 vs. #3 and #2 vs. #4, the increase of the conductances leads to an increase in the powder flow rates. The magnitude of the increase is larger with the longer powder line length. Carrier gas pressure also leads to an increase of the powder flow rates (experiment #1 vs. #5 and #3 vs. #6), and its impact was greater than that of changing the conductance for the cases tested here.

When comparing pulsed and continuous operation, namely, experiments #1 and #7, or #2 and #8, it is evident that the powder flow rate in pulsed operation was higher by a factor of at least two. This suggests that powder is injected more efficiently in pulsed mode for the types of supply systems studied here.

A comparison between experiments #1 and #2, or #3 and #4, shows the impact of the powder line length on the mass flows in pulsed operation. A longer length resulted in lower flow rates for both. On the other hand, in continuous operation, a comparison between experiments #7 and #8 shows that a longer line length produced higher powder flow rates while the gas flow rates were unaltered. This result is both unexpected and counterintuitive, as it suggests that longer powder lines improve system performance in continuous mode. Since the trend cannot continue indefinitely, an optimal point should exist that maximizes the powder flow rate for a given carrier gas flow rate. From a practical point of view, however, long powder lines are disadvantageous for microsatellites due to limited installation space. Also, the combustion chamber pressures exceed the supply pressure levels unless the propellants are stored in high-pressure vessels, but this would increase system complexity and

weight. Micropropulsion systems with pulsed powder supply have hence various advantages, and so the optimization of continuous powder supply was not pursued further in the present study.

The mass ratios, ϕ, for all experimental runs are shown in **Fig. 12** as a function of the carrier gas flow rate. In experiments #1–4, ϕ varied within the measurement uncertainty levels, making it difficult to identify a clear trend. This implies that the conductance and powder line length did not have significant impacts on ϕ for pulsed operation. On the other hand, the results of experiments #5 and #6 show that higher carrier gas pressures resulted in lower ϕ. Furthermore, ϕ was significantly lower in continuous operation than in pulsed mode. For the former, we found $106.7 \leq \bar{\phi}_{\mathrm{cont}} \leq 196.1$, while for the latter, we obtained $221.7 \leq \phi_{\mathrm{pulse}} \leq 413.7$.

In summary, the results imply that appropriate setting of the gas line conductance and selection of powder supply line length can control the powder flow rate without significant impacts on ϕ. They also imply that the short gas line length would be conservative considering the in-space operation of the supply system because it would be less affected by unexpected changes of gas line conductance and the flow rates can be controlled with the carrier gas pressure. Conversely, all variations of the carrier gas pressures constitute a trade-off between increased powder flow rates and decreased mass ratios ϕ. However, since the ϕ is very large even at high carrier gas pressures, the carrier gas is not expected to affect the reaction of the propellants in the combustion chamber. The propulsion system can hence be equipped with a capability of throttling. For instance, when a higher powder flow rate is required, perhaps for a short duration maneuver with high thrust, this can be achieved by an increase in the carrier gas pressure at the expense of reducing mass ratio.

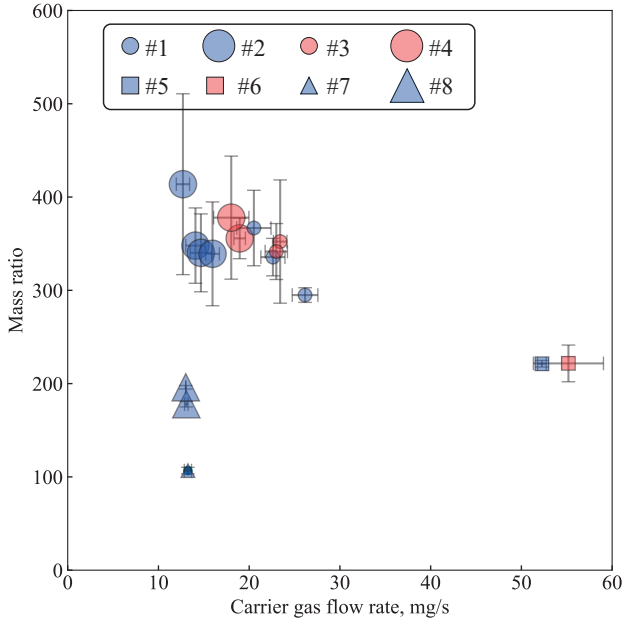

Fig. 12 Mass ratio ϕ versus gas flow rate.

4. Discussion

The flow rates were estimated with the assumption that the powder flow rate through the powder valve was constant during one shot. In what follows, the validity of this assumption is discussed first. Then, the mass ratio ϕ is expressed as a function of voidage, velocity ratio, and density ratio, which are variables that are commonly used to describe the flow fields of mixtures.

4.1 Flow field establishment

The time required by a particle to accelerate to the local flow speed can be expressed as

$$\tau_{\mathrm{a}} = \rho d_{\mathrm{p}}^2 / 18\mu \tag{16}$$

where d_{p} is the particle diameter, and μ is the carrier gas molecular viscosity. Using $\rho = 2{,}710$ kg/m^3, $d_{\mathrm{p}} = d_{50}$, and $\mu = 1.88 \times 10^{-5}$ Pa s, results in $\tau_{\mathrm{a}} \approx 1.5$ ms. Since $\tau_{\mathrm{a}} \ll \tau_{\mathrm{open}}$, the establishment time is much faster than typical time scale of valve response.

4.2 Reformulation of mass ratio

4.2.1 Definition of voidage, velocity ratio, and density ratio

Solid-gas mixture flows can be described by various parameters, including the pressure drop per unit length and the flow voidage. The pressure drop is not a critical issue in spacecraft because the supply lines are typically very short on the order of 10^{-2} m to 10^{-1} m. On the other hand, voidage is an indicator of the amount of carrier gas required to transport a certain amount of powder and is more important for spacecraft than for ground facilities. Another key factor of the mixture flow is the velocity ratio of the carrier gas and the powder from the perspective of the combustion. A lower velocity ratio indicates that the carrier gas goes through the combustion chamber at a relatively high velocity and powder can have sufficient residence time for a complete reaction. Therefore, we focus on the voidage and velocity ratio here.

A steady-state flow was assumed for both continuous and pulsed operation, as shown in **Fig. 13**, to derive the

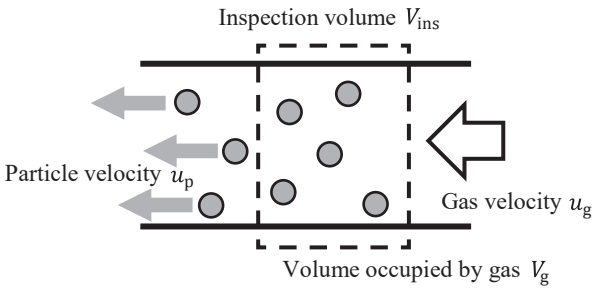

Fig. 13 Schematic of the steady-state flow inside the powder line.

relationship between the mass ratio and the voidage. Using the dispersed powder and gas mass density, ρ_{dp} and ρ_{dg}, respectively, and the inspection volume V_{ins}, the respective flow rates can be expressed as

$$\dot{m}_p = \rho_{dp} u_p A_{line} \quad (17)$$

$$\dot{m}_g = \rho_{dg} u_g A_{line} \quad (18)$$

where u_p and u_g are powder and carrier gas velocity, respectively, and A_{line} is the cross-sectional area of the powder line. Here, we can define the voidage as

$$\varepsilon \equiv V_g / V_{ins} = \rho_{dg} / \rho_g = 1 - \rho_{dp} / \rho_p \quad (19)$$

With the equations above, the mass ratio can be expressed as

$$\phi \equiv \frac{\dot{m}_p}{\dot{m}_g} = \frac{u_p}{u_g} \frac{1-\varepsilon}{\varepsilon} \frac{\rho_p}{\rho_g} \quad (20)$$

Eqn. (20) shows that ϕ can be expressed as a function of voidage ε, velocity ratio u_p/u_g, and density ratio ρ_p/ρ_g. The former two assume values in the range of 0–1. The mass ratio can be determined as outlined in **Section 2.5**. The density ratio can be estimated by using the measured carrier gas pressure in P3, and assuming that the gas temperature equaled room temperature, specifically, $T_g = 300$ K. Thus, the remaining unknown variables in **Eqn. (20)** are the voidage and the velocity ratio. Once either of them is estimated, the other can also be determined.

In continuous operation, we estimated the velocity ratio from the measurements as follows. First, the powder velocity u_p was calculated from

$$u_p = \frac{l_{t-p} + l_{p-c}}{t_{co} - \tau_{delay}} \quad (21)$$

The distance $l_{t-p} = 659$ mm between the tank exit and the powder valve was constant, while the distance l_{p-c} between the powder valve and collector tank inlet varied according to the experiment number (cf. **Table 2**). In **Eqn. (21)**, t_{co} is the time when the collector tank mass starts to increase, and $\tau_{delay} = 0.43$ s is the time delay of the mass scale. Here, $t = 0$ is the time when the powder valve opening commences. Next, the superficial carrier gas velocity u'_g was obtained from

$$u'_g \equiv \dot{m}_g / (\rho_g A_{line}) = \varepsilon u_g \quad (22)$$

using the known values for that $\dot{m}_g$, ρ_g, and A_{line}. Plugging **Eqn. (22)** into **Eqn. (20)** then yields

$$\phi = \frac{u_p}{u'_g}(1-\varepsilon)\frac{\rho_p}{\rho_g} \quad (23)$$

which can be rearranged to calculate ε.

In pulsed operation, the same estimation method cannot be used because the first injection was not in steady state. Thus, the voidage ε was estimated from the ratio between the total injected carrier gas volume in one shot, in steady state, and that after the powder discharge completed. This estimation assumes that the gas velocity was constant regardless of the powder existence in the flow. The total injected carrier gas volume in i^{th} pulse $V_{pulse,g,i}$ is

$$V_{pulse,g,i} = \int_{t_i}^{t_{i+1}} \dot{m}_g R_g T_g / p_g \mathrm{d}t \quad (24)$$

where R_g and p_g are the specific gas constant and the gas pressure, respectively. The values for $\dot{m}_g$ and p_g were measured by the flow meter and sensor P3, respectively. Using $R_g = 288.7$ J/ (kg K) for air and assuming $T_g = 300$ K as before, allowed the numerical integration of **Eqn. (24)** to yield $V_{pulse,g,i}$. For instance, in **Fig. 9**, pulses 10 to 24 were in steady state, while only carrier gas was injected in pulses 40–43. The average voidage in pulsed operation can then be obtained from

$$\varepsilon = \frac{\Sigma_{i=n_m}^{n_n} V_{pulse,p,i} / (n_n - n_m)}{\Sigma_{i=n_p}^{n_q} V_{pulse,p,i} / (n_q - n_p)} \quad (25)$$

where n_m and n_n are the first and last pulse number in the steady state, respectively, and n_p and n_q are the first and last pulse number, respectively, after stable periodic gas flow reestablished, such as for $t > 155$ s in **Fig. 8**. The result was then plugged into **Eqn. (20)** to obtain the velocity ratio.

4.2.2 Voidage and velocity ratio

The relation between the velocity ratio, u_p/u_g, and the voidage, ε, is shown in **Fig. 14**. This figure shows that the voidage in pulsed operation was in the range of 0.1–0.35, which indicates that 65–90% of the powder line volume was occupied by the powder. On the other hand, the voidage in continuous operation was approximately 0.8.

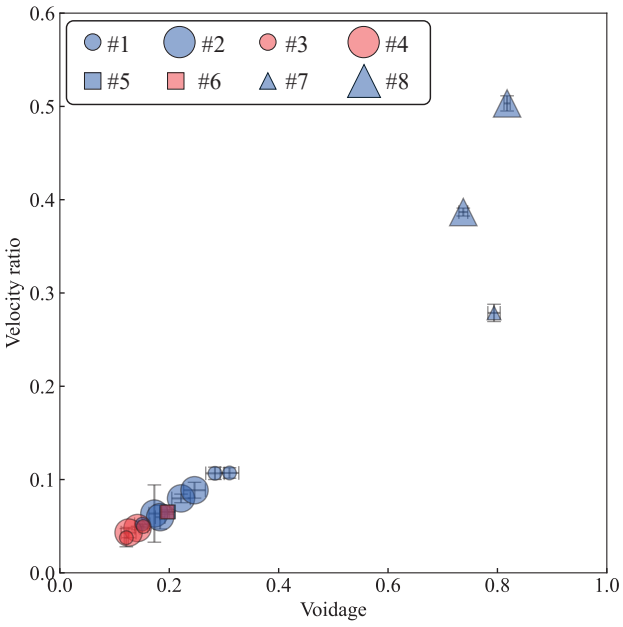

Fig. 14 Velocity ratio versus voidage. The symbols representing experiments #5 and #6 are overlapping.

The reason for this might be that the powder was compressed when the powder valve closed, and the flow was brought to a sudden halt (cf. **Section 3.1**) in pulsed operation. This effectively increased the powder packing density and reduced ε. Clearly, this effect is absent when the system is operated continuously. Also note that, for pulsed operation, a larger gas line conductance (experiments #3 and #4) contributed to denser powder flow (lower ε) when the supply pressure was kept constant (compare experiments #1 vs. #3 and #2 vs. #4). This figure clearly shows that pulsed supply is a preferable way for the powder transfer for micropropulsion application. Lower voidages indicate higher powder flow rates with lower carrier gas flow rates. Lower velocity ratios indicate lower powder velocities, resulting in longer residence times in a combustion chamber, thereby promoting complete combustion.

Differences in powder line length had a slight impact on the velocity ratio and voidage with lower gas line conductance (experiment #1 vs. #2) and did not have a significant impact on them (experiment #3 vs. #4). However, as shown in **Fig. 15**, the powder velocity was slower with a longer powder line length. This implies that the length can control the powder velocity without changing the mass ratio because **Fig. 12** shows that the length did not have an impact on ϕ. Slower powder velocities can result in a longer residence time of the powder in a combustion chamber and higher combustion efficiencies. Thus, a longer powder line, at least within length limits studied here, is advantageous for a micropropulsion system.

Comparing the data for experiments #1 and #5 in **Figs. 12**, **14**, and **15** helps assess the effect of carrier gas pressure. Experiment #5 shows lower voidage than experiment #1, whereas experiment #5 shows lower ϕ than experiment #1. This implies that the increase in the carrier gas mass density has a bigger impact than the decrease in the voidage. For this reason, higher carrier gas pressures can inject larger powder masses, but they will use disproportionally larger carrier gas masses.

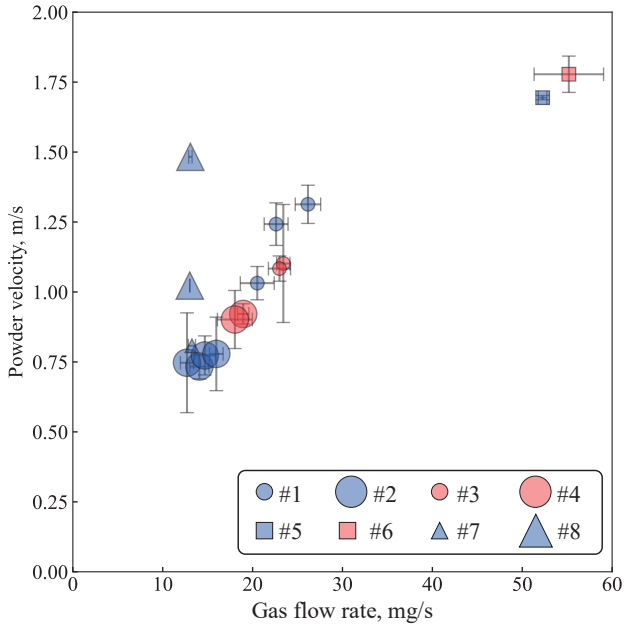

Fig. 15 Powder velocity versus gas flow rate.

Regarding the powder velocity in experiments #5 and #6, their velocities are significantly faster than in the other experiments, as shown in **Fig. 15**. Therefore, as a method to increase the injected powder mass per pulse, choosing higher carrier gas line conductances is preferable to selecting higher carrier gas pressures. This is because higher carrier gas pressures increase carrier gas consumption and reduce the residence time of the powder in the combustion chamber.

In summary, powder supply systems for micropropulsion applications require high mass ratios and low powder velocities. The former can be achieved with a higher carrier gas line conductance. The latter can be controlled by the powder line length without changing the mass ratio. Regarding the carrier gas pressure, it was clarified that lower pressures were beneficial because higher pressures reduced the mass ratio and increased powder velocities.

5. Conclusions

Powder supply systems for use in micropropulsion are technically immature, and important design parameters are not well studied. To overcome this, this study developed a powder supply system, and the impacts of carrier gas pressures, gas line conductances, and powder line lengths on the supply characteristics were measured.

The measurements were conducted in both continuous and pulsed operation modes. Experimental results indicated that pulsed operation achieved higher powder flow rates and higher mass ratios than continuous operation. Since achieving high mass ratios is critically important for a micropropulsion system, due to severely limited spacecraft mass budgets, pulsed operation mode is the preferable option for micropropulsion applications.

Furthermore, it was found that higher carrier gas supply pressures significantly increased the gas and powder flow rates, but at the same time reduced mass ratios. The carrier gas line conductance had a smaller impact on the powder flow rate, and only a negligible impact on the mass ratio. As a result, the carrier gas line conductance can be used as a design variable to control the former with only negligible impacts on the latter. The powder line length had a negative impact on the powder flow rate, but it had no significant impact on the mass ratio.

The results implied that the appropriate design of the gas line conductance and the powder line length can control the powder flow rate, and the carrier gas pressure is an effective parameter to control the powder flow rates in-space operation for throttling. The results provided important insights and help for the future development of

micropropulsion systems that use aluminum powder, or indeed physically similar metal powders, as fuels. It should be noted that the measurements were carried out under $1g_0$. The validation of the results under microgravity conditions will be performed in a future drop tower experiment.

Acknowledgments

This work was financed through the European Space Agency (ESA) Open Discovery Channel on the ESA Open Space Innovation Platform (OSIP) as project I-2022-05117. This support is gratefully acknowledged. The authors would also like to thank Matthew Smith at ESA-ESTEC, TEC-MPC, for supporting this study in his role as technical officer. Lead author also appreciates former financial support by a Japanese Society for the Promotion of Science (JSPS) KAKENHI Grant (Grant-in-Aid for JSPS Fellows, No. 21J20721).

Nomenclature

ABS	Acrylonitrile butadiene styrene
CAD	Computer-aided design
ESA	European Space Agency
JSPS	Japanese Society for the Promotion of Science
OSIP	Open Space Innovation Platform
PSD	Particle size distribution
SRM	Solid rocket motor
d_t	inner diameter of powder tank (m)
d_x	x^{th} percentile diameter (m)
F	force (N)
g_0	gravitational acceleration, 9.8 (m/s^2)
h	height of powder bed (m)
I	current (A)
$m_{Al,ini}$	initial aluminum powder mass (kg)
$\dot{m}_{cont,g}$	carrier gas flow rate during continuous operation (kg s^{-1})
$\dot{m}_{cont,p}$	powder flow rate during continuous operation (kg s^{-1})
$m_{c,i}$	collector tank mass before i^{th} shot during pulsed operation (kg)
$\dot{m}_g$	carrier gas flow rate measured by the flow meter (kg s^{-1})
$m_{pulse,p,i}$	injected powder mass in i^{th} shot during pulsed operation (kg)
$m_{pulse,g,i}$	injected carrier gas mass in i^{th} shot during pulsed operation (kg)
$\dot{m}_{pulse,p,i}$	powder flow rate in i^{th} shot during pulsed operation (kg)
$\dot{m}_{pulse,g,i}$	gas flow rate in i^{th} shot during pulsed operation at powder valve (kg)
$\bar{m}_{pulse,g}$	averaged injected carrier gas mass during one shot in pulsed operation (kg)
$\bar{m}_{pulse,p}$	averaged injected powder mass during one shot in pulsed operation (kg)
$\bar{\dot{m}}_{cont,g}$	averaged carrier gas flow rate during continuous operation (kg s^{-1})
n_m	first pulse number in steady state (-)
n_n	last pulse number in steady state (-)
n_p	first pulse number after steady state (-)
n_q	last pulse number after steady state (-)
t_i	time when i^{th} powder valve is opened (s)
N	number of coil turns (-)
ε	voidage inside powder line (-)
ε_t	voidage inside powder tank (-)
μ	molecular viscosity (Pa s)
ρ	density (kg m^{-3})
σ	standard deviation (-)
σ_d	size polydispersity (-)
τ_a	time required by a particle to accelerate to the local flow speed (s)
τ_{delay}	time delay of mass scale measurement (s)
τ_{open}	time during which the powder valve is open (s)
$\phi_{pulse,i}$	mass ratio in i^{th} shot during pulsed operation (-)
$\bar{\phi}_{cont}$	average mass ratio during continuous operation (-)
$\bar{\phi}_{pulse}$	average mass ratio during pulsed operation (-)

References

Besenhard M.O., Fathollahi S., Siegmann E., Slama E., Faulhammer E., Khinast J.G., Micro-feeding and dosing of powders via a small-scale powder pump, International Journal of Pharmaceutics, 519 (2017) 314–322. https://doi.org/10.1016/j.ijpharm.2016.12.029

Cocco R., Chew J.W., 50 years of Geldart classification, Powder Technology, 428 (2023) 118861. https://doi.org/10.1016/j.powtec.2023.118861

David A.O., Knoll A.K., Experimental demonstration of an aluminum-fueled propulsion system for CubeSat applications, Journal of Propulsion and Power, 33 (2017) 1320–1324. https://doi.org/10.2514/1.B36330

Foote J.P., Thompson B.R., Lineberry J.T., Combustion of aluminum with steam for underwater propulsion, in: Gabriel D. Roy (Ed.), Advances in Chemical Propulsion: Science to Technology, CRC Press LLC, New York, 2001, pp. 133–145, ISBN: 9780429128820. https://doi.org/10.1201/9781420040685

Geldart D., Types of gas fluidization, Powder Technology, 7 (1973) 285–292. https://doi.org/10.1016/0032-5910(73)80037-3

JIS B2005-1, Industrial-process control valves - part 1: control valve terminology and general considerations, Japanese Standards Association, 2004.

Li C., Zhu X., Deng Z., Yang J., Hu C., Wei J., Powder feeding in a powder engine under different gas-solid ratios, Acta Astronautica, 189 (2021) 712–721. https://doi.org/10.1016/j.actaastro.2021.08.022

Miller T.F., Herr J., Green rocket propulsion by reaction of Al and Mg powders and water, 40th AIAA/ASME/SAE/ASEE Joint Propulsion Conference and Exhibit, American Institute of Aeronautics and Astronautics, 2004. https://doi.org/10.2514/6.2004-4037

Miller T.F., Walter J.L., Kiely D.H., A next-generation AUV energy system based on aluminum-seawater combustion, in: Proceedings of the 2002 Workshop on Autonomous Underwater Vehicles, presented at the Symposium on Autonomous Underwater Vehicle Technology (AUV), IEEE, 2002, pp. 111–119.

Morikawa Y., Progress of technology in powder transportation: pneumatic and hydraulic conveying, Tetsu-to-Hagane, 77 (1991) 480–489. https://doi.org/10.2355/tetsutohagane1955.77.4_480

Murohara M., Koizumi H., Zhang R., Nishii K., Komurasaki K., Experimental study on combustion of water vapor and aluminum powder for chemical micropropulsion, Transactions of the Japan Society for Aeronautical and Space Sciences, 67 (2024) 86–98. https://doi.org/10.2322/tjsass.67.86

Nishii K., Koizumi H., Temperature measurement on condensed combustion products of magnesium with oxygen and water vapor, Combustion and Flame, 262 (2024) 113362. https://doi.org/10.1016/j.combustflame.2024.113362

Ogata K., A review: recent progress on evaluation of flowability and floodability of powder, KONA Powder and Particle Journal, 36 (2019) 33–49. https://doi.org/10.14356/kona.2019002

Ogata K., Ariga D., Evaluation of flowability for granulated powder using a test of powder discharge by pressurized air, EPJ Web of Conferences, 249 (2021) 08001. https://doi.org/10.1051/epjconf/202124908001

Oh K.W., Rong R., Ahn C.H., Miniaturization of pinch-type valves and pumps for practical micro total analysis system integration, Journal of Micromechanics and Microengineering, 15 (2005) 2449. https://doi.org/10.1088/0960-1317/15/12/029

Qian G.-H., Bágyi I., Burdick I.W., Pfeffer R., Shaw H., Stevens J.G., Gas–solid fluidization in a centrifugal field, AIChE Journal, 47 (2001) 1022–1034. https://doi.org/10.1002/aic.690470509

Risha G.A., Connell T.L., Yetter R.A., Sundaram D.S., Yang V., Combustion of frozen nanoaluminum and water mixtures, Journal of Propulsion and Power, 30 (2014) 133–142. https://doi.org/10.2514/1.B34783

Ruiz-Carcel C., Starr A., Nsugbe E., Estimation of powder mass flow rate in a screw feeder using acoustic emissions, Powder Technology, 336 (2018) 122–130. https://doi.org/10.1016/j.powtec.2018.05.029

Sun H., Hu C., Zhang T., Deng Z., Experimental investigation on mass flow rate measurements and feeding characteristics of powder at high pressure, Applied Thermal Engineering, 102 (2016) 30–37. https://doi.org/10.1016/j.applthermaleng.2016.03.142

Sundaram D.S., Yang V., Zarko V.E., Combustion of nano aluminum particles (Review), Combustion, Explosion, and Shock Waves, 51 (2015) 173–196. https://doi.org/10.1134/S0010508215020045

Wollmark S., Yavor Y., Burning rates of nanoaluminum–water solid propellants at various pressures, Journal of Propulsion and Power, 35 (2019) 173–181. https://doi.org/10.2514/1.B37098

Xu H., Gao J., Zhong W., Zhu H., Experimental study on the fluidization discharging characteristics of Geldart-C kaolin powders in a blow tank with pulsed gas, Advanced Powder Technology, 33 (2022) 103372. https://doi.org/10.1016/j.apt.2021.11.024

Authors' Short Biographies

Dr. Masaya Murohara is a postdoctoral researcher at Zurich University of Applied Sciences (ZHAW) and a specialist in the field of chemical micropropulsion system. He was awarded Ph.D. by the University of Tokyo in 2024, having been involved in the development, management, testing, and operation of a micropropulsion system installed on a 6U CubeSat, EQUULEUS. He proposed a novel microchemical propulsion system utilizing water and metal powder, and is currently engaged in its R&D in collaboration with the University of Tokyo, Sirin Orbital Systems AG, and the Europe Space Agency.

Dr. Marius Banica is a Principal Lecturer and head of research/focus area energy efficiency at Zurich University of Applied Sciences (ZHAW). He was awarded Ph.D. by University of Cambridge in 2007 and subsequently held the position of postdoctoral researcher at University of Stuttgart (2007–2009), propulsion engineer at Airbus (2009–2012), senior research and development engineer at ABB (2012–2019), and then commenced his tenure at ZHAW in 2019. His expertise lies in the field of fluid engineering, with a particular focus on simulation.

Prof. Hiroyuki Koizumi is an Associate Professor in the department of advanced energy and department of aeronautics and astronautics at the University of Tokyo, Japan, where he directs the space propulsion laboratory and leads the developments of micro-propulsion systems for microsatellites: Hodoyoshi-4, PROCYON, AQT-D, and EQUULEUS. He was awarded Ph.D. by the University of Tokyo in 2006, and held the position of an Assistant Professor in JAXA (2007–2011) and Associate Professor in the University of Tokyo (2011–). He also is a co-founder and member of the board of the space propulsion startup Pale Blue Inc.

Dr. Matteo Madi is an entrepreneur, innovator, business developer and space-tech specialist with over fifteen years of work experiences in the Swiss and International public and private sectors. He is the founder of Sirin Orbital Systems AG, a Swiss innovative company based in Zurich, focused on the development and commercialization of advanced enabling technologies for the needs of emerging space market and future sustainable space exploration. As Managing Director at Sirin Orbital Systems AG, Dr. Madi also contributes to the creation of innovative solutions for the use of space technologies and satellite-based services for terrestrial applications.